1 **A platform of patient-derived microtumors identifies treatment**
2 **response and therapeutic vulnerabilities of ovarian cancer.**

3 Nicole Anderle[1]*, André Koch[2], Berthold Gierke[3], Anna-Lena Keller[1], Annette Staebler[4],
4 Andreas Hartkopf[2], Sara Y. Brucker[2,5], Michael Pawlak[3], Katja Schenke-Layland[1,2,5,6,7],
5 Christian Schmees[1]*

6

7 [1]NMI Natural and Medical Sciences Institute at the University of Tuebingen, Reutlingen, 72770
8 Germany.
9
10 [2]Department of Women's Health, Eberhard Karls University Tuebingen, Tuebingen, 72076
11 Germany.
12
13 [3]NMI Technologie Transfer GmbH, Pharmaservices Protein Profiling, Reutlingen, 72770
14 Germany.
15
16 [4]Institute of Pathology and Neuropathology, Eberhard Karls University Tuebingen, Tuebingen,
17 72076 Germany.
18
19 [5]Cluster of Excellence iFIT (EXC2180) "Image-Guided and Functionally Instructed Tumor
20 Therapies", Eberhard Karls University Tuebingen, Tuebingen, 72076 Germany.
21
22 [6]Department of Biomedical Engineering, Eberhard Karls University Tuebingen, 72076 Tuebingen,
23 Germany.
24
25 [7]Department of Medicine/Cardiology, Cardiovascular Research Laboratories, David Geffen
26 School of Medicine at UCLA, Los Angeles, CA, 90095 USA.
27
28
29 * Nicole Anderle, Christian Schmees
30 **Email:** nicole.anderle@nmi.de, christian.schmees@nmi.de

31

32

33

34

35

36

37

38

Abstract

Ovarian cancer (OvCa) is an insidious disease: due to nonspecific symptoms, these tumors are usually diagnosed at advanced stage with correspondingly devastating consequences for treatment outcome and patient survival. The broad heterogeneity of OvCa manifests itself in the complex composition of the tumor microenvironment. Given the frequent development of therapeutic resistance, there is a strong need for model systems accurately representing OvCa heterogeneity, while enabling parallel drug testing and prediction of appropriate treatment responses in individual patients. Here, we demonstrate the efficient isolation of highly viable OvCa patient-derived microtumors (OvCa PDM). Importantly, our data demonstrate histopathological comparability of OvCa PDM with corresponding patient tumor tissue. Reverse phase protein array (RPPA)-based analyses of >110 total and phospho-proteins enabled the identification of sensitivities to standard, platinum-based as well as experimental, selumetinib-based therapy, and thereby the prediction of treatment-responder. Parallelized drug testing in OvCa PDM allowed functional validation of RPPA data and detection of on- and off-target treatment effects. Strikingly, clinical follow-up of corresponding patients confirmed significantly increased metastasis-free survival of identified carboplatin-responder. Furthermore, flow cytometry-based characterization of autologous TIL populations confirmed the presence of tumor-specific, cytotoxic TILs with stem-like CD39$^-$PD1$^+$ and terminally differentiated CD39$^+$PD1$^+$ phenotypes. Interestingly, our results showed a significant correlation between the presence of CD8$^+$CD39$^+$ Tils and lymph node metastasis in the associated patients. Finally, combining OvCa PDM and autologous TILs for efficacy testing of immune checkpoint inhibitors demonstrated the potential for patient-specific enhancement of cytotoxic TIL activity by this therapeutic approach.

Main Text

Introduction

Ovarian cancer (OvCa) is among the most lethal gynecological diseases in women with a 5-year survival rate of ~30% for advanced stage compared to 92% for the early diagnosed localized, primary disease state [1]. In view of dismal treatment success rates, substantial efforts have been made to resolve the complexity of OvCa, especially for high-grade serous carcinomas (HGSC). Despite the success of genomics and transcriptomics in elucidating disease determinants, the principles of OvCa responsiveness to therapy are still poorly understood [2].

In this context, patient-derived model systems are expected to play an important role in order to identify suitable and effective therapies for the individual patient as well as existing therapeutic resistances of the patient's tumor. Even though recent studies have described the combination of PDO cultures with components of the tumor microenvironment including fibroblasts, endothelial cells and immune cells [3], PDOs do not reflect the original composition of primary tumor tissue in terms of extracellular matrix, tumor-associated fibroblasts, tumor-infiltrating lymphocytes (TILs), macrophages (TAMs), and tumor endothelial cells. Another challenge of current PDO models in terms of applicability for individualized tumor response testing relates to the required establishment time of 1-3 months with a corresponding impact on the timeframe to obtain drug testing results [4].

Here, we introduce a three-dimensional (3D) preclinical OvCa model composed of patient-derived microtumors (PDM) as well as autologous tumor-infiltrating lymphocytes (TIL) isolated from primary OvCa tissue specimen in a clinical relevant time-frame. PDM recapitulate a 3D histo-architecture with retained cell-cell contacts and native intra-tumoral heterogeneity featuring the corresponding primary tumor microenvironment (incl. extracellular matrix proteins, stromal fibroblasts and immune cells). In combination with functional compound efficacy testing and multiplexed TIL phenotyping, we assessed the correlation of individual OvCa PDM responses to chemotherapeutic, targeted as well as immunotherapeutic treatment approaches using OvCa PDM alone and in co-culture with autologous TILs, respectively. We used Reverse Phase Protein

90 Array (RPPA) analysis to map protein-signaling pathways of PDM and to measure on- and off-
91 target pathway effects in compound treated PDM. Strikingly, a correlation of obtained data in
92 OvCa PDM models with clinical follow-up data of corresponding patients showed a significant
93 increase in metastasis-free survival of identified carboplatin-responder as compared to non-
94 responder.

95 **Results**
96
97 **Isolation of highly viable patient-derived microtumors from primary OvCa tissue samples**
98 **by limited enzymatic digestion**
99
100 Residual fresh tumor tissue samples were collected from n = 19 patients suffering from OvCa and
101 undergoing primary tumor debulking surgery. Available, anonymized clinicopathological
102 characteristics including International Federation of Gynecology and Obstetrics (FIGO) staging
103 and pathological TNM-classification of respective individuals are summarized in Table S1. 2/19
104 patients (OvCa #4 and OvCa #18) received neoadjuvant treatment with carboplatin/paclitaxel
105 chemotherapy. The majority of included samples (n = 17) were derived from the most common
106 type of OvCa, i.e. epithelial OvCa, with a majority of high-grade serous carcinomas (HGSC). Two
107 samples were classified as sex-chord-stromal ovarian carcinomas that are either non-malignant
108 or at a low stage. PDM isolation adapted from Kondo *et al.* 2011 [5] and TIL isolation was
109 performed on freshly excised tumor tissue specimen. Isolation of PDM amounts suitable for
110 downstream analyses was successful in >70% (14/19) of the tumor samples (Fig. 1A). PDMs
111 were cultured in suspension in the absence of serum for a maximum of three weeks. No
112 correlation was observed between successful isolation of PDM and available clinical patient data
113 such as age, lymph node spread, distant cancer spread, perineural invasion or FIGO stage
114 (Table S2). PDM viability was assessed by parallel staining with Calcein-AM and SYTOX™
115 Orange (Fig. 1B). 2D projections of 3D images displayed highly viable PDM with few dead cells.
116 Dead PDM cells (according to nuclear SYTOX™ Orange staining) were detached from PDM and
117 thus observed mostly as single cells floating in the culture media. The quantification of the viable
118 cell volume and dead cell volume in 3D projections of four exemplary OvCa PDM models are
119 shown in Fig. 1C. In each analyzed model, ≤ 7% of the total PDM cell mass represented dead
120 cells confirming robust PDM viability.
121
122 **OvCa PDM sections resemble histopathological characteristics of the corresponding**
123 **primary tumor tissue (PTT)**
124
125 We next performed Hematoxylin and Eosin staining (H&E) of FFPE- and cryosections,
126 respectively, derived from OvCa PDM and corresponding primary tumor tissue sections (PTT) for
127 histopathological comparison. Professional assessment of PDM by a certified pathologist,
128 confirmed typical, distinct histopathological characteristics of OvCa (Fig. 1D and Fig. S1). HGSC
129 derived PDM reflected architectural patterns such as papillary growth, irregular branching, cystic
130 and glandular structures (Fig. 1D OvCa #17-23; Fig. S1, OvCa #24, 26) as compared to the
131 corresponding PTT specimen. Pleomorphic nuclei/cells, high nucleus:cytoplasm ratio as wells as
132 hyperchromasia were similar in PDM and corresponding PTT sections reflecting the high-grade of
133 analyzed HGSC tumors. These tumor features were not detected within OvCa PDM #8 (Fig. S1),
134 which originated from low-grade mucosal OvCa known for slow tumor growth. Instead, OvCa #8
135 PDM displayed a unicellular epithelium and mostly stromal remains. In summary,
136 histopathological analyses of PDM confirmed structural and cellular similarities to the
137 corresponding primary tumor specimen resembling typical histological features of ovarian
138 carcinomas.
139
140
141
142

PDMs reflect intra- and intertumoral heterogeneity of the original tumor

143
144
145 For further characterization and study of the similarity of OvCa PDM and corresponding PTT, the
146 expression of histotype specific markers, different tumor cell-, extracellular matrix- and immune
147 cell-markers were assessed by immunohistochemistry (Fig. 1D, Fig. S1). In the clinics,
148 immunohistochemical staining of p53 and Wilms Tumor 1 (WT1) is applied for differential
149 diagnosis of HGSCs [6]. HGSC phenotype of the original tumor persists in the corresponding PDM
150 as marker expression of WT1/p53 highly corresponded with either low-to-moderate (OvCa #17-
151 18) or strong expression (OvCa #23). Mesothelin (MSLN) and CA125 (MUC16) were used as
152 additional OvCa markers. Mesothelin, known to be over-expressed on the cell surface in OvCa [7-
153 9], was readily expressed in OvCa PDM resembling expression of this marker in their
154 corresponding PTT. Besides MSLN, CA125 expression has previously been described as an
155 immunohistochemical marker to confirm ovarian origin of the tumor [10]. As shown before [11,12],
156 expression of CA125 in OvCa sections can vary within one type and between the different OvCa
157 tumor types. Accordingly, PTT sections derived from non-HGSC displayed no CA125 expression
158 (OvCa #8) in contrast to HGSC-derived tumor sections (OvCa #17-18, #23-26). In PDM models
159 OvCa#8, #17, #18 and #24 staining patterns of MSLN and CA125 were similar to corresponding
160 PTT sections and were often restricted to cells at the tumor margin for CA125 (e.g. OvCa #18,
161 #23). As the tumor microenvironment is known to play a major role in tumor progression and
162 metastasis [13-15], we analyzed the presence of extracellular matrix (ECM) and stromal components
163 in OvCa PDM and corresponding PTT. Sections were stained for FAPα (Fibroblast associated
164 protein alpha), a marker of activated fibroblasts, also known as cancer-associated fibroblasts
165 (CAFs). FAPα expression in tumor stroma is observed in 90% of human cancers of epithelial
166 origin and has been described to induce tumor progression and chemoresistance [16]. FAPα
167 staining in OvCa PDM mostly resembled that of the corresponding PTT in all samples except for
168 OvCa #24-26 and differed from low to high expression. Collagen I expression, known to promote
169 invasiveness and tumor progression in epithelial OvCa [17], was also prominent within OvCa PDM.
170 Stainings correlated with corresponding PTT that showed an overall strong Collagen I expression
171 except for OvCa #25. We also observed a strong correlation of Hyaluronan Binding Protein 1
172 (C1QBP) expression in PDM and corresponding PTT, which interacts with the major ECM
173 component hyaluronan [18]. In summary, all studied stromal components were found to be highly
174 abundant within OvCA PDM and corresponding PTT. To further examine tumor
175 microenvironmental (TME) components of PDM, we studied the infiltration with tumor-associated
176 macrophages (TAMs) via CD163 expression together with the expression of the inhibitory
177 checkpoint receptor ligand PD-L1. Analysis rarely detected M2-like TAMs (CD163$^+$) within PTT
178 and PDM sections and if so, mostly in stromal tissue parts. While macrophages were highly
179 frequent in OvCa #24 PTT, they were not detected in the corresponding PDM (Fig. S1). In
180 contrast, for OvCa #17, CD163$^+$ TAMs were detected in both PDM and PTT sections (Fig. 1).
181 Immune checkpoint receptor ligands are known to be expressed on tumor and/or immune cells of
182 the tumor microenvironment. Here, PD-L1 expression was mostly absent in OvCa PTT and
183 corresponding PDM sections. In conclusion, PDM largely resembled features of the original tumor
184 by direct comparison with corresponding PTT including presence of complex ECM and TME
185 architecture and expression of markers specific for OvCa. In comparison with corresponding PTT
186 sections, pure stromal areas were mostly absent from stained PDM sections, which might explain
187 differences observed between PDM and corresponding PTT with regard to immune cell infiltration
188 and degree of expression of stromal components.
189
190 **Protein signaling pathway profiling of OvCa PDM by RPPA**
191
192 After initial immunohistochemical characterization of the 3D OvCa PDM that confirmed the
193 presence of TME components in PDM similar to corresponding PTT, we performed an in-depth
194 examination of the heterogeneity and molecular composition of different OvCa PDM models by
195 generating complete signaling pathway protein profiles using RPPA. Protein abundances of 116
196 different proteins (including total and post-translationally modified forms) were measured in OvCa

4

197 PDM samples each with a sample size of n = 100-150 per individual PDM (Fig. 2A). One further
198 PDM sample derived from human BC (breast cancer) was included to scale up the protein
199 sample data and for comparison as both cancer types are known to share molecular and
200 microenvironmental similarities [15,19]. Obtained protein-normalized, background-corrected mean
201 fluorescence intensity (NFI) signals were median-centered to all samples (n = 8) and log_2
202 transformed. Protein profiles of PDM samples covered signaling pathways such as for cell cycle,
203 DNA damage response, apoptosis, chromatin regulation, MAPK/RTK, PI3K/AKT with mTOR, Wnt
204 and NFκB, as well as OvCa tumor/stem cell markers. By hierarchical clustering (HCL), PDM were
205 grouped according to their similarities in relative protein signal intensity (Fig. 2A). Data analysis
206 revealed three clusters: 1) OvCa #21 (OvCa granulosa cell tumor) and #23 (HGSC), with the
207 most distinct protein profiles as compared to the other PDM analyzed; 2) OvCa #19 (HGSC) and
208 the BC PDM shared more similarities then OvCa #19 with the other OvCa PDM models; 3). The
209 remaining PDM samples resembled the third cluster with the most similar protein expression
210 profiles containing exclusively HGSC models. Long distances of the sample dendrogram further
211 underlines the proteomic heterogeneity of similar histopathological OvCa tumor types.
212 To compare protein abundances within different signaling pathways as well as of tumor/stem cell
213 markers, proteins with impact on pathway activity were sorted according to their pathway
214 affiliation (Fig. 2B, Table S3). Significant differences between PDM models were observed for the
215 cell cycle pathway and the MAPK/RTK pathway. Highest cell cycle activity was found in OvCa
216 #17 and #24 with almost 50% higher median NFI signals compared to OvCa #21 with the lowest
217 median signals (median NFI = -0.33 log_2) resembling a different histopathological tumor type
218 compared to the other PDM models analyzed. MAPK/RTK pathway signaling was increased in
219 OvCa #21 (median NFI = 0.38 log_2), #23 (median NFI= 0.32 log_2), #24 (median NFI = 0.31 log_2)
220 and #17 (median NFI = 0.30 log_2). The BC PDM model was characterized by decreased median
221 NFI signals of MAPK/RTK proteins (median NFI = -0.47 log_2). Proteins related to PI3K/AKT
222 pathway and of associated pathways were more abundant in OvCa #17 and #24. mTOR pathway
223 levels were elevated in OvCa #24 (median NFI = 0.54 log_2) in other OvCa PDM this pathway
224 showed comparable activity. Median NFI signals from apoptosis-related proteins were
225 significantly different between OvCa #25 (median NFI = 0.75 log_2) and BC PDM (median NFI=
226 1.41 log_2). OvCa tumor/stem cell marker protein abundance was significantly upregulated in both
227 OvCa #17 and #23 compared to BC PDM. RPPA protein profiling analysis demonstrated the
228 heterogeneous activity of several signaling pathways within different OvCa PDM. Apoptosis-
229 related proteins and OvCa tumor/stem cell marker proteins indicated the strongest differences
230 between OvCa PDM models and the BC PDM model.
231
232 **Heterogeneous treatment responses towards chemo- and targeted therapy assessed by**
233 **functional compound testing in OvCa PDM**
234
235 Next, we used OvCa PDM as a platform for functional compound testing using standard-of-care
236 chemotherapy treatment and targeted therapies. Further, we sought to relate treatment
237 responses in PDM to the generated protein profiling datasets. Studies of targeted therapies in
238 OvCa are often limited to clinical phase I and II or even cell-line based preclinical studies [20-22], as
239 treatment efficacies are heterogeneous and mostly not beneficial compared to standard
240 chemotherapy. However, targeting specific signaling pathways could demonstrate a treatment
241 alternative for individual OvCa patients either as first-line or recurrent-cancer therapy. As we have
242 discovered that protein abundances differed the most in the cell cycle and MAPK/RTK pathway in
243 OvCa PDM (Fig. 2A-B), we investigated efficacy of targeted inhibition of these pathways with the
244 CDK4/6 inhibitor palbociclib, the MEK1/2 inhibitor selumetinib, as well as the Src-inhibitor
245 saracatinib and compared these treatments to standard platinum-based chemotherapy (Fig. 2C).
246 PDM were treated with respective drugs, each at three different concentrations, chosen according
247 to previously reported C_{max} concentrations [23]. Treatment efficacy in OvCa PDM – as measured by
248 cytotoxicity - was heterogeneous among individual PDM models, with some specifically
249 responding to carboplatin (most prominently OvCa #24) and others to targeted therapy (OvCa
250 #19, #21, #26). Carboplatin induced the most significant cytotoxic effects at the lowest dose (75

5

251 µM) at longest duration t = 72 h in OvCa #17 and #24 (Fig. 2C). On the molecular level, RPPA
252 protein profiling revealed significantly increased cell cycle activity in both models (Fig. 2B), which
253 might be associated with the stronger carboplatin response observed in OvCa PDM #17 and #24.
254 Two other PDM models were also carboplatin sensitive, but responded to treatment at higher
255 dose (OvCa #23, #25). Accordingly, both had shown intermediate cell cycle activity in protein
256 profiling analyses (Fig. 2A-B). Selumetinib induced significant cell death in OvCa #17, #19, #21
257 and #23 at a final concentration of 100-150 nM (Fig. 2C). The strongest effect was observed for
258 OvCa #21, which displayed comparatively high MAPK/RTK pathway activity (Fig. 2B). Palbociclib,
259 an inhibitor of G1-cell cycle progression, caused significant cytotoxicity in OvCa #25 and #26,
260 which both had shown moderate cell cycle activity in RPPA protein analysis (Fig. 2B). PDM
261 models with significantly higher cell cycle activity as measured by RPPA (OvCa #17, #24), did not
262 respond to palbociclib treatment. Inhibition of the Src-pathway by saracatinib caused significant
263 and dose-dependent killing effects in OvCa #26. Saracatinib triggered rapid PDM death already
264 after 24-48 h of treatment. In conclusion, functional compound testing further confirmed the
265 molecular heterogeneity of studied OvCa PDM models identified by protein profiling. Interestingly,
266 PDM models showing resistance to standard chemotherapy with carboplatin were instead
267 sensitive towards targeted therapeutic approaches.
268
269 **Correlation of treatment response and activation state of protein signaling pathways**
270
271 To relate the analyzed protein signaling pathways of untreated OvCa PDM to observed treatment
272 responses, protein NFI signals of PDM were grouped into responder and non-responder profiles
273 according to results from functional compound testing (Fig. 2C, Fig. S2). Significant differences of
274 pathway signaling in carboplatin/selumetinib responder and non-responder models were
275 analyzed. Further, we examined the on- and off-target pathway effects within different OvCa PDM
276 models by RPPA to assess drug mode-of-action (Fig. 3). For this aim, OvCa PDM were treated at
277 one compound concentration and compared to vehicle (DMSO) control. Treatment-to-control
278 signal ratios (TR) were determined from protein NFI signals of treated PDM samples and DMSO
279 vehicle controls at three different time points for each treatment: immediate (30 min), early (4 h)
280 and late (72 h). This enabled the exploration of fast and late treatment response based on
281 changes of protein abundances within a given time frame.
282
283   **Carboplatin treatment sensitivity of OvCa PDM correlates with high protein**
284   **abundance of G2-M cell cycle proteins**
285
286 HCL clustering of PDM protein NFI signals led to five clusters that distinguish carboplatin
287 sensitive and resistant PDM models (Fig. S3A). To analyze significant differences related to
288 activation or inactivation of signal transduction pathways, proteins from the HCL clustering were
289 sorted according to their pathway affiliation and according to upregulation or downregulation in
290 responder. Carboplatin-responder showed significantly increased cell cycle activity ($P < 0.001$;
291 Fig. 3A) with upregulated protein abundance observed for Aurora A kinase (mean NFI = 0.74
292 $\log_2$), CDK2 (mean NFI = 0.8 $\log_2$), Cyclin B1 (mean NFI = 0.84 $\log_2$), PCNA (mean NFI = 0.84
293 $\log_2$), and acetylated Tubulin (mean NFI = 0.1 $\log_2$) (Fig. S3B), which are mostly related to
294 "mitosis" [24,25]. Aurora A (Spearman's r = 0.912, P = 0.022), Cyclin B1 (Spearman's r = 0.971, P =
295 0.011) and PCNA (Spearman's r = 0.912, P = 0.022) significantly correlated with carboplatin
296 treatment sensitivity (Table S4), which was graded according to recorded significance levels from
297 0-3 ("0": $P > 0.05$; "1": $P < 0.05$; "2": $P < 0.01$; "3": $P < 0.001$) (Fig. S2). At the same time, non-
298 responder showed higher abundance of CDK1 (mean NFI = 0.38 $\log_2$), phospho-CDK2 (mean
299 NFI = 0.77 $\log_2$) and phospho-CDK4 (mean NFI = 0.37 $\log_2$) (Fig. S3C), which are more related to
300 the G0/G1 cell cycle phase. In addition, the apoptosis/DNA damage response pathway was
301 significantly upregulated in responder OvCa PDM models compared to non-responder (P =
302 0.021; Fig. 3A), especially with high abundance of cleaved Caspase-8 and cleaved PARP (Fig.
303 S3B). Additional significant differences between responder and non-responder OvCa PDM were
304 detected within the RTK and the PI3K/AKT/NFκB signaling pathways ($P < 0.001$; Fig. 3A). These

305 pathways were downregulated in the non-responder group. Higher EMT/tumor/CSC marker
306 abundance was significantly associated with the carboplatin responder group (Fig. 3A). Markers
307 included Mesothelin, Nanog, STAT1, and E-Cadherin (Fig. S3B). In contrast, there were few
308 proteins found, which were downregulated in the responder group. Collectively, this panel of
309 downregulated proteins differed significantly compared to the non-responder group (Fig. 3A). It
310 contained early cell cycle markers e.g. Aurora A and Cyclin B1, the mTOR pathway effector
311 phospho-S6RP, PDGFR and SNAI1 (Fig. S3C). In summary, the activation state of different
312 signaling pathways comprised of proteins with >20% difference in abundance, allowed to
313 significantly distinguish carboplatin responder from non-responder OvCa PDM models.
314
315 **Carboplatin treatment is associated with early induction of stress-response and**
316 **late apoptosis**
317
318 Next, we sought to investigate the carboplatin drug mode-of-action within OvCa PDM. Therefore,
319 the carboplatin-responding OvCa PDM #24 was treated with carboplatin at a concentration of
320 75 µM, which had significantly induced PDM cytotoxicity (see Fig. 2C). Protein NFI signals were
321 measured at three different time points and normalized to vehicle control. Proteins revealing
322 >50% difference in TR signals (Fig. S4) were selected to focus on the strongest changes in
323 abundance. Cell cycle progression proteins (phospho-CDK2, CDK1) and phospho-Histone H3
324 (Ser10), affecting chromatin condensation during cell division, were downregulated quickly within
325 30 minutes (Fig. 3B). After 4 h of treatment, TR signals of phospho-Aurora A/B/C protein and
326 Histone H3 was strongly increased (Fig. S4). Longer incubation with carboplatin (72 h) resulted in
327 strong downregulation of these proteins (Fig. 3B). Diminished abundance of cell cycle proteins
328 after 72 h of carboplatin treatment differed significantly from vehicle control ($P < 0.001$) and from
329 early treatment (4 h; $P < 0.001$). While levels of cell cycle related proteins decreased over time,
330 apoptotic markers such as cleaved-Caspases as well as acetylated p53 were elevated after 72 h
331 (Fig. S4). Induction of apoptosis-related proteins was already observed after 4 h of treatment (Fig.
332 3B) with increasing abundances of cleaved Caspase 7 and acetylated p53 (Fig. S4). Focusing on
333 down-stream PI3K/AKT/mTOR/Wnt pathway regulation, the abundances of mTOR effector
334 proteins (S6RP, S6RP-phospho) were quickly upregulated after immediate (0.5 h) carboplatin
335 treatment (Fig. S4), which is in line with previous reports about transcriptional regulation of stress
336 response by the mTOR pathway [26]. We also observed additional elevation of mTOR pathway-
337 related proteins after 4 h of carboplatin treatment. Furthermore, overactive mTOR signaling might
338 have resulted in increased p53 activation through increased acetylated p53 levels (Fig. S4) as
339 described before [26]. The PI3K/AKT/mTOR pathway was significantly upregulated within 4 h of
340 carboplatin treatment compared to vehicle control ($P = 0.021$; Fig. 3B). Similar to proteins related
341 to cell cycle, this pathway was completely abrogated as compared to vehicle control after 72 h of
342 treatment ($P < 0.001$; Fig. 3B). Changes in protein abundance differed significantly during all
343 three measured time points (0.5 h vs. 4 h: $P = 0.003$; 4 h vs. 72 h and 0.5 h vs.72 h: $P < 0.001$
344 Fig. 3B). Complete, significant downregulation of MAPK/RTK pathway occurred after 72 h of
345 treatment ($P = 0.017$; Fig. 3B). The proteomic changes within MAPK/RTK-related proteins over
346 time were significant (0.5 h vs. 4 h: $P = 0.009$; 4 h vs. 72 h: $P < 0.001$; Fig. 3B). Thus, carboplatin
347 treatment of OvCa #24 illustrated substantial and time-dependent changes in TR signals. Short
348 treatment with carboplatin apparently triggered the induction of stress responses while longer
349 treatment duration caused the induction of apoptosis.
350
351 **Metastasis-free-survival prolonged in carboplatin responder group**
352
353 To assess the predictive value of OvCa PDMs and obtained drug testing data, we compared
354 metastasis-free-survival (MFS) between carboplatin responder (OvCa #17, #23-25) and non-
355 responder (OvCa #19, #26) (Fig. S5). For this, OvCa PDM models were classified according to
356 carboplatin-responses measured by PDM functional compound testing (Fig. S2). Following
357 consideration of clinical follow-up patient data survival analyses revealed a significant difference
358 between carboplatin responder and non-responder. Carboplatin-responder had a prolonged

359 median MFS of 494 days (16.2 month) versus 281 days (9.2 month) in non-responder. Thus,
360 functional compound testing of OvCa PDM might enable treatment response prediction of
361 platinum-based standard chemotherapy in corresponding ovarian cancer patients.
362
363 **Selumetinib responding OvCa PDM models display increased MAPK/RTK pathway**
364 **activity**
365
366 HCL cluster analysis by Euclidean distance distinguishes selumetinib responder and non-
367 responder OvCa PDM models by six clusters (Fig. S6A). By sorting these proteins according
368 to pathway affiliation, selumetinib responder PDM models showed significantly increased
369 MAPK pathway (e.g. Erk1/2) and RTK pathway proteins (e.g. PDGFRβ) compared to non-
370 responder PDM in line with previous reports from cell line-based studies [27] ($P < 0.001$; Fig. 3C
371 and Fig. S6B). Another protein cluster consisting of diverse pathway proteins such as the cell
372 cycle, EMT markers or tumor markers showed significantly higher NFI signals compared to non-
373 responder PDM models ($P < 0.001$; Fig 3C and Fig. S6B). In contrast, one cluster was defined by
374 increased NFI signals within non-responder PDM with significantly upregulated proteins related to
375 cell cycle/DNA damage response (e.g. cleaved Caspases, phospho-CDK4), MAPK signaling
376 (phospho-EGFR (Tyr1068)), PI3K/AKT signaling and associated pathways such STAT and Wnt
377 signaling ($P < 0.001$; Fig. 3C and Fig. S6C). Similar to previous cell line studies [27,28] we detected
378 a number of potential selumetinib resistance features such as high levels of phospho-EGFR
379 (Tyr1068) and an active PI3K/AKT pathway in non-responder PDM models. By grouping the
380 proteins from HCL clustering according to pathway affiliation and abundance levels, we were able
381 to distinguish responder from non-responder PDM models. Especially a more active MAPK/RTK
382 pathway and a less active PI3K pathway allowed for the differentiation of responder from
383 selumetinib-resistant, non-responder PDM models.
384
385 **Upregulation of MAPK/RTK and PI3K/AKT signaling pathways in response to**
386 **selumetinib treatment as a potential resistance mechanism**
387
388 We next evaluated on- and off-target pathway effects by RPPA protein profiling of selumetinib-
389 treated OvCa models to assess potential resistance mechanisms. As data were available from
390 selumetinib responder (OvCa #17 and #21) and non-responder (OvCa #24) PDM models, protein
391 abundances after treatment were compared for those groups. Protein abundances were
392 measured as TR signals at three different treatment durations to track protein changes over time
393 (Fig. 3D). Proteins with 100% differential mean TR signals between these groups were selected
394 (Fig. S7-S9) and sorted according to pathway affiliation. While shortly after 4 h of treatment
395 responder PDM models upregulated specific cell cycle and apoptosis proteins (Fig. 3D) incl.
396 cleaved Caspase 7, phospho-CDK2 ($P = 0.017$) and phospho-Histone H3 (Ser10) (Fig. S7), non-
397 responder PDM models significantly upregulated cell cycle proteins after 72 h of treatment ($P <$
398 0.001; Fig. 3D). Proteins showing increased abundance are involved in G0/G1- and G2/M-cell
399 cycle progression such as Aurora A, phospho-CDK4, phospho-CDK6, phospho-Rb, phospho-
400 CDK2 (Fig. S7). In contrast to a progressing cell cycle within non-responder PDM models,
401 selumetinib induced a cell cycle arrest and apoptosis in the responder PDM group accompanied
402 by upregulation of phospho-CDK2 [29], the effector cleaved Caspase 7 and p53 (Fig. S7). After 72
403 h of treatment, analyses identified a significant difference in the activity of the MAPK/RTK
404 pathway, which was directly affected by the treatment with the MEK1/2 inhibitor ($P = 0.004$; Fig.
405 3D). Treatment did not affect the MAPK/RTK pathway activity in the non-responder group.
406 Instead, our data showed a time-dependent increase in MAPK/RTK activity (Fig. 3D, S8). In line
407 with reports about the influence of PI3K/AKT/NFκB/Wnt signaling on resistance to selumetinib
408 treatment in cell lines [27,28,30], we detected a significant upregulation of proteins related to these
409 pathways within the non-responding OvCa PDM after 4 h ($P = 0.003$) and 72 h ($P < 0.001$) of
410 treatment (Fig. 3D, S9). Non-responder PDM models showed a downregulation of the AKT-
411 inhibitor PTEN over time accompanied by increased phospho-AKT and Wnt signaling proteins
412 such as β-catenin, phospho-GSK3β (Fig. S9). At the same time, PI3K/AKT/NFκB/Wnt signaling

8

413 proteins were substantially decreased following selumetinib treatment in responder PDM models
414 (Fig. 3D). Thus, parallel upregulation of PI3K/AKT/NFκB/Wnt and MAPK/RTK signaling might
415 illustrate a potential resistance mechanism in selumetinib non-responder OvCa PDM models.
416
417 Characterization of tumor-infiltrating lymphocyte populations from primary OvCa tissue
418 samples
419
420 Our established procedure of tissue processing and PDM isolation enabled us to obtain single-
421 cell suspensions containing tumor-infiltrating lymphocytes (TILs) from respective OvCa tumor
422 specimen. This allowed for expansion of these autologous TILs in the presence of low-dosed
423 cytokines and antigenic stimulation in order to investigate the immunogenicity of our patient
424 samples. The immunogenicity of OvCa has been demonstrated in prior studies and is confirmed
425 by the frequent infiltration of ovarian tumors with TILs [31-33]. As reported by Sato *et al*. (2005),
426 different T cell populations diversely influence tumor immunosurveillance in OvCa. High
427 intraepithelial CD8$^+$/CD4$^+$ T cell ratios in patients were associated with improved survival as CD4$^+$
428 T cells executed immunosuppressive functions. To determine the composition of the isolated
429 immune cell infiltrate within our sample cohort, we characterized the phenotype of autologous TIL
430 populations by multi-color flow cytometry (Fig. S10A). Within isolated and expanded OvCa TIL
431 populations from different specimen, we found that the proportion of CD4$^+$ TILs was 57.8% and
432 significantly more abundant than CD8$^+$ TILs with 33.5% (P = 0.003**; Fig. 4A, Table S5). As
433 higher CD8:CD4 ratios were previously correlated with better survival in OvCa patients [31,33], the
434 majority of patients in this cohort were characterized rather with an unfavorable prognosis (Fig.
435 S10B).
436

438 Isolated CD8$^+$ OvCa TILs are comprised of tumor-specific CD39$^+$, stem-like CD39$^-$PD1$^+$ and
439 terminally differentiated CD39$^+$PD1$^+$ populations
440
441 Within the isolated CD8$^+$ TIL populations, we identified different phenotypes according to
442 expression of the co-inhibitory receptors PD-1 and CTLA-4, the tumor-antigen specificity marker
443 CD39 and the activation marker CD137 (Fig. 4A). To investigate the activation status of CD8$^+$
444 TILs, cells were examined for co-expression of the co-stimulatory receptor CD137 (4-1BB).
445 CD137 is upregulated in activated T cells and has been suggested to be a marker for antigen-
446 activated T cells [34]. The mean percentage of CD8$^+$ CD137$^+$ TILs was 3.1% and varied between 0-
447 10% (Table S5). >5% of the CD8$^+$ cytotoxic T-cells (CTLs) from OvCa #1, #3 and #5 (Fig. S10B)
448 co-expressed CD137 indicating their pre-exposure to tumor antigens. Expression of co-inhibitory
449 receptors PD-1 and CTLA-4 on CD8$^+$ TILs did not differ significantly among analyzed TIL
450 populations but tended to higher PD-1 expression levels (mean 6.9% vs. 3.4%; Table S5). TILs
451 from OvCa #3, #7 and #25 as well as #5, #13 and #26 were among those displaying an
452 exhausted phenotype with >10% of CD8$^+$PD-1$^+$ or CD8$^+$CTLA-4$^+$ TILs (Fig. S10). Moreover, in
453 recent reports CD39 expression in CD8$^+$ TILs was described as a marker for tumor-antigen
454 specific TILs that have undergone tumor-antigen-driven clonal expansion, exhibit resident
455 memory T cell like phenotypes and express a variety of co-stimulatory and co-inhibitory receptors
456 [35-37]. Here, CD39$^+$ CTLs (mean 40.5%; range 4.4-96.8%, Table S5) were significantly
457 more abundant than CD39$^-$ CTLs (mean 9.5%; range 0-48.3%, Table S5) so called 'bystander
458 TILs' known to recognizing mostly viral antigens [36] (P < 0.001, Fig. 4A). The amount of CD39$^+$
459 TILs strongly correlated with the amount of CD8$^+$ TILs (Spearman r = 0.88, Fig. S10C; P < 0.001,
460 Table S6) and conversely with the amount of CD4$^+$ TILs (Spearman r = -0.80, Fig. S10C; P =
461 0.002, Table S6). Thus, the abundance of CD4$^+$ and CD8$^+$ TILs appeared to significantly
462 determine the amount of CD39$^+$ CTLs. In addition, CD39 expression was largely limited to CD8$^+$
463 TILs. As co-inhibitory receptors play a role in T cell exhaustion and are important targets for
464 immune checkpoint-inhibition, we analyzed PD-1 and CTLA-4 expression on the tumor-specific
465 CD39$^+$ CTL population. PD1$^+$CD39$^+$ were more frequent than CTLA-4$^+$ CD39$^+$ (15.7% vs. 5.4%
466 Fig. 4A, Table S5). The total amount of CD8$^+$PD1$^+$ TILs thereby correlated with the amount of

9

467 CD8$^+$CD39$^+$PD1$^+$ TILs (Spearman r = 0.79, Fig. S10C; P = 0.002, Table S6) of a PDM model.
468 Thus, CD39 expression was limited to tumor-antigen stimulated and exhausted TILs (e.g. OvCa
469 #7, #17 and #25; Fig. S10B). In contrast to 'terminally differentiated cells' [38], OvCa TILs with a
470 'stem cell-like' CD39$^-$PD1$^+$ phenotype were found in 7.3% of the CTLs (Table S5). This population
471 showed the highest proportional variability with a maximum of 50.5% cells vs. a minimum of 0%
472 as compared to other CD8$^+$ TIL populations (CV 208%). The frequency of CD8$^+$CD39$^+$ and stem
473 cell-like CD8$^+$CD39$^-$PD1$^+$ was negatively correlated (Spearman r = -0.63, Fig. S10C; P = 0.024,
474 Table S6).
475
476 **Specific TIL phenotypes isolated from OvCa tumor specimen correlate with regional lymph**
477 **node metastasis**
478
479 We further analyzed the correlation between specific TIL populations and clinical follow-up patient
480 data. OvCa patients with regional lymph node metastasis (N = 1) tended to present with
481 significantly more extensive CD8$^+$ TIL infiltration in their tumors than those with no lymph node
482 metastasis (N = 0) (P = 0.016) (Fig. 4B). As the frequency of CD8$^+$ TILs was shown to
483 significantly correlate with that of CD8$^+$CD39$^+$ TILs in OvCa (Fig. 4B), our data implicate a
484 significant correlation between lymph node spread (N=1) and the presence of a CD8$^+$CD39$^+$
485 population (P = 0.008).
486
487 **OvCa PDM killing by autologous TIL populations is enhanced by immune checkpoint**
488 **inhibitor treatment**
489
490 To evaluate the functional, tumor cell killing capacity of autologous TILs on OvCa PDM and the
491 corresponding treatment efficacy of established immune checkpoint inhibitors (CPI), we subjected
492 co-cultures of TILs and PDM from OvCa #24 and #26 to image-based analysis of
493 CPI-treatment response. A total of nine PDM were imaged per treatment (3 PDM per well in
494 triplicates) and a dead:live PDM ratio was calculated according to the sum of measured
495 fluorescent intensities (FI) (Fig. 4C-E). Addition of TILs to autologous PDM induced a basal killing
496 effect in PDM in both models analyzed in the absence of CPI treatment (Fig. 4D-E). For both co-
497 culture models analyzed, the addition of CPI led to an increase in PDM cell death. Significantly
498 higher killing effects in OvCa #24 co-cultures were observed in response to treatment with either
499 the combination of anti-PD1 and anti-CTLA-4 (pembrolizumab + ipilimumab) or anti-PD-L1 and
500 anti-CTLA-4 (atezolizumab + ipilimumab) (P = 0.039) compared to isotype control treatment (Fig.
501 4D). As the addition of isotype controls showed no additional effect in both co-culture models, we
502 excluded the possibility of unspecific killing effects of CPI antibodies. CPI treatment almost
503 doubled PDM killing in OvCa #26 (Fig. 4E). In comparison, co-cultures treated with ipilimumab (P
504 = 0.004) or atezolizumab (P < 0.001) showed significant PDM killing compared to untreated PDM.
505 The killing effect of TILs was significantly amplified by atezolizumab treatment as compared to co-
506 culture controls (PDM+TIL: P = 0.021; PDM+TIL+IgG4: P = 0.018; Fig. 4E). Further,
507 atezolizumab treatment significantly increased the TIL killing effect towards PDM as compared to
508 pembrolizumab (P = 0.026). Taken together, autologous TILs from both OvCa PDM models
509 studied were composed of high amounts of tumor-specific, non-terminally differentiated
510 CD8$^+$CD39$^+$ TIL populations (Fig. S10B) inducing PDM killing. Especially TILs from OvCa #26
511 responded with enhanced PDM killing to CPI treatment. Thus, co-culture assays of autologous
512 TILs and PDM offer a platform to assess CPI treatment efficacies in a preclinical, patient-specific
513 setting.

514 **Discussion**
515
516 In the present study, we introduce a platform of PDM and autologous TILs extracted by limited
517 enzymatic digestion from a panel of primary OvCa tissue specimen. Our results show a 70%
518 success rate for isolation of PDM with robust viability and in suitable amounts for further, multi-
519 parametric downstream analyses. In-depth histopathological assessment of PDM sections

10

520   confirmed the conservation of typical histological features of respective OvCa types by this model
521   system. Importantly, the complexity of the ovarian cancer TME with respect to the presence of
522   cancer-associated fibroblasts and extracellular matrix components incl. collagen and hyaluronan-
523   binding protein observed in primary OvCa tissue sections was well reflected in PDM. The
524   presence of these TME components has previously been correlated with tumor stage, prognosis,
525   and progression and shown to substantially influence treatment responses [17,39,40]. Interestingly,
526   we could also identify immune cell infiltration within a subset of OvCa PDM, reflecting the
527   immunogenicity of OvCa as previously reported [31,32,41].
528   While OvCa patient-derived organoids (PDO) were often studied by genomic and transcriptomic
529   sequencing [42-44], we were the first (to our knowledge) to investigate inter-tumoral heterogeneity
530   and differential drug response mechanism by RPPA-based protein profiling in a patient-derived
531   3D OvCa preclinical model.
532   Here, analyses of a panel of >110 phospho- and total proteins allowed for the clustering of
533   histologically similar OvCa PDM models, pathway activity profiling and investigation of on- and off
534   target drug effects. Obtained RPPA protein profiles confirmed the heterogeneity of OvCa PDM
535   observed via immunohistochemistry and previously reported for HGSC, the most common type of
536   OvCa. Our work identified significant differences in the activity of cell cycle and MAPK/RTK
537   pathways within analyzed OvCa PDM and enabled their distinction from a breast cancer derived
538   PDM model by differential expression of OvCa tumor and stem cell markers as well as apoptosis-
539   related proteins.
540   Seven OvCa PDM models were applied for individualized compound efficacy testing using a
541   panel of clinically approved drugs at C_{max} drug concentrations previously reported in clinical trials.
542   For analyzed OvCa PDM models, we observed patient-specific heterogeneity of response
543   towards chemotherapy and targeted therapy. Correlation with RPPA protein profiling data allowed
544   the allocation of individual PDM drug responses to specifically up- or down-regulated signaling
545   pathway activities and, importantly, enabled the prediction of PDM models with high probability of
546   response towards chemotherapy or targeted therapy.
547   In accordance with the ability of cytostatic drugs to induce apoptosis especially in actively dividing
548   cells [45], our work identified additional correlation between proteins relevant for S- and G2/M- cell
549   cycle phase progression and carboplatin response. Specifically, our data implicate that elevated
550   abundances of Aurora A, Cyclin B1 and PCNA proteins may allow for identification of carboplatin
551   treatment response. Furthermore and in line with previous reports, we confirmed that decreased
552   DNA damage repair and the ability to undergo apoptosis [46] is associated with carboplatin
553   treatment sensitivity in OvCa. This was illustrated by increased levels of cleaved Caspase-7 and
554   cleaved PARP. Our results did not identify a correlation of carboplatin-resistance and markers of
555   cancer stem cells (CSCs) [47,48] or epithelial-to-mesenchymal transition (EMT) [49,50]. Instead, we
556   found the cancer stem cell-related protein Nanog as well N-Cadherin strongly upregulated in
557   carboplatin responding PDM. These differing results might arise from the fact that above-
558   mentioned previous studies were performed in adherent cell lines and not within a patient-derived
559   3D tumor model. Importantly, we identified protein signatures of OvCa PDM allowing for the
560   identification and prediction of PDM models with high probability of response towards
561   chemotherapy or targeted therapy. Strikingly, our results showed a significant correlation of
562   carboplatin treatment response with prolonged metastasis-free survival of respective patients.
563   The targeted inhibition of MEK1/2 kinase by selumetinib induced cell death within different OvCa
564   PDM models. Treatment responses to selumetinib have yet been clinically evaluated with a focus
565   on LGSC patients, because of observable MAPK pathway activation in this type of OvCa.
566   However, reported clinical response rates were limited. Nevertheless, different studies identified
567   relationships between phospho-EGFR (Y1068) and phospho-Erk with selumetinib sensitivity
568   [27,28,30,51]. In line with this, our study identified selumetinib-sensitive PDM models by means of
569   moderate MAPK/RTK pathway activity with increased abundance of Erk1/2, PDGFR and other
570   proteins. Furthermore, our results imply a central role of active PI3K/AKT/mTOR signaling and
571   upregulated caspase protein levels in selumetinib treatment resistance.
572   We further assessed proteomic changes upon PDM treatment such as effects on protein
573   abundance, directed on- and off-target pathway effects and drug mechanism-of-action within

574 OvCa PDM. In a carboplatin sensitive PDM model, we observed a time-dependent decrease in
575 cell cycle- and an increase in apoptosis-inducing protein abundance. In parallel, we found a fast
576 stress response upon treatment as indicated by an activated mTOR pathway with high S6RP and
577 active phospho-S6RP levels [26]. Overactive mTOR in combination with cell stress and the inability
578 of cells to adapt to cellular stress might be responsible for p53 elevation [52,53] and driving cells into
579 senescence or apoptosis [54,55]. The degree of mTOR activation and the severity of stress in form
580 of carboplatin-induced DNA damage might indicate the failure of PDM to induce protective
581 responses and thus treatment-sensitivity.
582 With the comparison of on- and off-target pathway effects in selumetinib-sensitive and –resistant
583 OvCa PDM models, we uncovered significant changes in protein abundance for responder versus
584 non-responder PDM models during treatment. In line with previous reports, on-target pathway
585 effects of selumetinib treatment were characterized by a reduction in MAPK/RTK pathway protein
586 levels accompanied by the induction of cell cycle arrest and apoptosis by high cleaved Caspase7,
587 p53 and phospho-CDK2 levels[29]. Selumetinib treatment resistance was characterized on the one
588 hand by MAPK feedback signaling with increased abundance of RTKs such as phospho-EGFR
589 and upregulated AKT and Wnt-signaling by means of high phospho-AKT and β-catenin levels.
590 Active PI3K/AKT/Wnt pathway signaling in OvCa PDM might indicate resistance to the MEK-
591 inhibitor selumetinib as reported earlier [27,28,30].
592 Apart from testing the response of OvCa PDM to conventional therapy, we also applied
593 immunophenotyping of autologous TIL populations followed by their co-culture with respective
594 PDM for assessment of individualized responses towards immunotherapeutic mono- and
595 combination treatment schedules. Immunosurveillance of cancer strongly depends on the
596 composition of tumor-infiltrated immune cells and the degree of tumor tissue infiltration and is
597 known to influence treatment efficacies. As a result, the idea of an immunoscore, identifying a
598 patient's immunophenotype, emerged [56]. Our work uncovered several immunophenotypes within
599 expanded TILs from OvCa patients by multicolor flow cytometry compared to previous
600 immunohistochemistry based analysis [57]. As described by Sato *et al*. (2005) [31] and Zhang *et al*.
601 (2003) [32] high numbers of intraepithelial CD8$^+$ TILs are associated with better prognosis in OvCa.
602 We found that OvCa TILs were largely composed of CD4$^+$ rather than CD8$^+$ TILs. In this regard,
603 OvCa models with high amounts of suppressive CD4$^+$ TILs and low numbers of CD8$^+$ TILs are
604 suggested to have worse prognosis [58]. In line with previous reports [59], we identified expression of
605 CD39 in OvCa TIL populations, a marker that distinguishes between tumor-specific CTLs (CD39$^+$)
606 and bystander TILs (CD39$^-$) [35,36]. Interestingly, we found that CD8$^+$ TIL amounts correlated with
607 that of CD8$^+$ CD39$^+$ TILs, and could confirm that these tumor-specific T cells constitute an
608 exhausted, memory T cell like phenotype, as CD39 expression was limited to CD8$^+$PD-1$^+$ TILs.
609 Importantly, our results further demonstrated that co-cultures of PDM and autologous TILs could
610 be applied to assess the treatment effect of CPIs in a preclinical and patient-specific setting. Such
611 PDM-TIL co-culture systems could potentially be used to identify OvCa patients, who would most
612 likely benefit from immunotherapies. According to the data presented here, OvCa tumors with
613 regional lymph node metastasis contained higher numbers of CD8$^+$ and CD8$^+$CD39$^+$ TILs. The
614 co-culture models tested in our study for response towards CPI treatment were derived from
615 lymph-node spreading primary tumors, which might suggest that immunogenicity of OvCa
616 increases upon metastasis.
617 Limitations of our PDM model are currently the restricted number of PDM available from digestion
618 of individual tumor tissue samples. From experience with different tumor types, an average of
619 several hundred to several thousand microtumors can be isolated from fresh tissue samples. This
620 number depends on the amount of tissue available for PDM isolation as well as tissue
621 composition (including degree of fibrosis and necrosis). PDMs are therefore presently not suitable
622 for high-throughput drug screening approaches, but for focused drug testing in late preclinical and
623 translational drug development as well as in the context of precision oncology. Since PDM
624 generally show a low proliferation rate in culture, passaging and propagation of these models is
625 currently not feasible; at the same time, it should be considered that dissociation during
626 passaging of PDM would probably dissolve their valuable tissue-like structure and would be

627 accordingly disadvantageous. Similar to patient-derived tumor organoids, PDM can be
628 cryopreserved and thus applied in repetitive analyses.
629 In line with the present study on OvCa PDM, our recent work on PDM established from human
630 glioblastoma tissue specimen showed a good histopathological comparability of PDM with
631 corresponding primary tumor tissue [60,61] and contained, among other components of the tumor
632 stroma, tumor-associated macrophage populations, which are crucial for the response shown
633 towards treatment with CSF1R and PD1 targeting antibodies [60]. The expansion of currently
634 existing interactions with clinical centers will be of crucial importance for the further successful
635 implementation of this test system in future applications of precision oncology.
636
637 **Materials and Methods**
638
639 **Human specimens**
640
641 Ovarian tumor samples were obtained from nineteen patients diagnosed with ovarian cancer
642 undergoing surgery at the Center for Women's Health, University Hospital Tuebingen. Written
643 informed consent was obtained from all participants. The tumors were classified according to
644 International Federation of Gynecology and Obstetrics (FIGO) grading system. Tumor samples
645 were delivered on the day of operation. The research project was approved by the ethics
646 committee (IRB#275/2017BO2 and IRB#788/2018BO2).
647
648 **Isolation and cultivation of patient-derived microtumors and tumor-infiltrating**
649 **Lymphocytes**
650
651 The procedure was adapted from Kondo et al. (2011) (Kondo, 2011 #200) and modified as
652 follows. Tumor specimens were washed in HBSS (Gibco), minced with forceps, and digested with
653 LiberaseTM DH (Roche) for 2h at 37°C. Digested tissue was centrifuged (300g, 5 min), washed
654 with HBSS and filtered through a stainless 500 µm steel mesh (VWR). The flow-through was
655 again filtered through a 40 µm cell strainer (Corning). The filtrate containing the TIL fraction was
656 resuspended in Advanced RPMI 1640 (Gibco) supplemented with 2 mM Glutamine (Gibco), 1%
657 MEM Vitamins (Gibco), 5% human serum (Sigma-Aldrich) and 100 µg/ml primocin (Invivogen).
658 IL-2 (100 U/ml), IL-7 (10 U/ml) and IL-15 (23.8 U/ml) (Peprotech) were freshly added to culture
659 media. For expansion, CD3/CD28 dynabeads were added (Milteny Biotech). PDM, held back by
660 cell strainer, were washed in HBSS and cultured in suspension in StemPro® hESC SFM (Gibco)
661 supplemented with 8 ng/ml FGF-basic (Gibco), 0.1 mM β-mercaptoethanol (Gibco), 1.8% BSA
662 (Gibco) and 100 µg/ml primocin (Invivogen) within cell-repellent culture dish (60x15 mm)
663 (Corning).
664
665 **RPPA and protein data analysis**
666
667 Detailed methods of sample preparation and RPPA processing are provided in SI Materials.
668 RPPA protein analysis and protein data processing was applied as reported before [62-64]. Detailed
669 methods of sample preparation and RPPA processing are provided in SI Materials. From the
670 arrays, PDM sample signals were extracted as protein-normalized, background-corrected mean
671 fluorescence intensity (NFI), as measured from two technical sample replicates. NFI signals,
672 median-centered for each protein over all measured samples (including OvCa PDM and BC PDM
673 samples) and log2 transformed, reflect a measure for relative protein abundance. Small NFI
674 protein signals at around blank assay level (0.02 NFI) were as a limiting quality criterion excluded
675 from further analysis; otherwise all NFI signals were used for further protein data analysis. Protein
676 heat maps were generated and cluster analysis (HCL) performed using the freely available
677 MultiExperiment Viewer (MeV) software. For the comparison of protein profiles of treatment
678 responders and non-responders (defined by functional compound testing; Fig. 3C, Fig. S2), only
679 proteins with a >20% difference between the means were used for analysis. On- and off-target
680 pathway effects were evaluated from one biological and two technical replicate samples per

681 model at three different treatment times (0.5, 4 and 72 h). Treated sample to respective DMSO
682 vehicle control NFI ratios (TR) were calculated for each treatment condition and log2-
683 transformed.
684 If possible, the protein abundances were shown as mean of responder/non-responder or both
685 (analyzed beforehand by functional compound testing; Fig. 2C). A treatment-specific threshold of
686 protein change (carboplatin: minimum 50% difference; selumetinib: minimum 100% difference)
687 was set. Only proteins showing treatment effects above the threshold were shown.
688
689
690 **Efficacy of compounds validated in PDM cultures**
691
692 Efficacy of compounds was validated by applying the real-time CellTox™ Green Cytotoxicity
693 assay (Promega). Assays were performed according to manufacturer's protocol. PDM were
694 cultured a maximum of 1-2 weeks in PDM culture medium prior testing. Per treatment three to
695 eight replicates were performed using n = 15 PDM per replicate in a total volume of 150 µl
696 phenol-red free PDM culture medium. Cell death was measured as relative fluorescent unit (RFU)
697 (485–500 nm Ex / 520–530 nm Em), relative to the number of dead, permeable cells after 24h,
698 48h and 72h with the Envision Multilabel Plate Reader 2102 and Tecan Spark Multimode Plate
699 Reader. RFU values were normalized to DMSO control or H_2O control according to used drug
700 solvent. Treatment effects were measured as fold change (FC) compared to control. Differences
701 between treated PDM and untreated PDM were calculated as fold change values separately for
702 each time point. Statistical significance was evaluated by two-way ANOVA multiple comparison
703 test. Outliers were identified with the Iglewicz and Hoaglin's robust test for multiple outliers
704 applying a recommended Z-score of ≥ 3.5 [65].
705
706 **Statistical analysis**
707
708 Statistical analysis was performed using GraphPad Prism. For Boxplot data, whiskers represent
709 quartiles with minimum and maximum values and the median. Datasets with no clear normal
710 distribution were analyzed with unpaired, two-tailed Mann-Whitney-U-test, otherwise as indicated.
711 Correlation data were evaluated by Spearmans rank correlation. For all analyses, *P* values < 0.05
712 were considered statistically significant. Recommended post-hoc tests were applied for multiple
713 comparisons.
714
715 **Data and materials availability**
716
717 All data and materials are available upon request after signature of an MTA from the
718 corresponding authors.
719
720 **Acknowledgments**
721
729
730 **Author Contributions**
731
732 Conceptualization: N.A, C.S, M.P, K.SL, S.Y.B, A.H,
733 Methodology: N.A, B.G, M.P, AL.K
734 Investigation: N.A, B.G, M.P, A.K, AL.K, A.S, S.Y.B,

735 Project administration: N.A, C.S, A.K
736 Supervision: C.S, A.K
737 Writing – original draft: N.A, C.S
738 Writing – review & editing: N.A, C.S, M.P, AL.K, K.SL, A.K, S.Y.B, A.H, A.S
739
740 **Competing Interest Statement**

741 Andreas Hartkopf received consulting and speaking fees from GSK, AstraZeneca and Clovis.
742 Nicole Anderle, André Koch, Berthold Gierke, Anna-Lena Keller, Annette Staebler, Sara Y.
743 Brucker, Michael Pawlak, Katja Schenke-Layland and Christian Schmees report no conflicts of
744 interest.

745
746 **References**
747

748 1 Surveillance, Epidemiology and End Results (SEER) Program (www.seer.cancer.gov)
749 SEER*Stat Database: Incidence - SEER Research Data, 9 Registries, Nov 2020 Sub
750 (1975-2018) - Linked To County Attributes - Time Dependent (1990-2018)
751 Income/Rurality, 1969-2019 Counties, National Cancer Institute, DCCPS, Surveillance
752 Research Program, released April 2021, based on the November 2020 submission.
753 (National Cancer Institute, Bethesda, MD).
754 2 Zhang, H. *et al.* Integrated Proteogenomic Characterization of Human High-Grade
755 Serous Ovarian Cancer. *Cell* **166**, 755-765, doi:10.1016/j.cell.2016.05.069 (2016).
756 3 Neal, J. T. *et al.* Organoid Modeling of the Tumor Immune Microenvironment. *Cell* **175**,
757 1972-1988.e1916, doi:10.1016/j.cell.2018.11.021 (2018).
758 4 Wensink, G. E. *et al.* Patient-derived organoids as a predictive biomarker for treatment
759 response in cancer patients. *npj Precision Oncology* **5**, doi:10.1038/s41698-021-00168-1
760 (2021).
761 5 Kondo, J. *et al.* Retaining cell-cell contact enables preparation and culture of spheroids
762 composed of pure primary cancer cells from colorectal cancer. *Proc. Natl. Acad. Sci. U.*
763 *S. A.* **108**, 6235-6240, doi:10.1073/pnas.1015938108 (2011).
764 6 Köbel, M. *et al.* An Immunohistochemical Algorithm for Ovarian Carcinoma Typing. *Int. J.*
765 *Gynecol. Pathol.* **35**, 430-441, doi:10.1097/pgp.0000000000000274 (2016).
766 7 Hilliard, T. The Impact of Mesothelin in the Ovarian Cancer Tumor Microenvironment.
767 *Cancers (Basel)* **10**, 277, doi:10.3390/cancers10090277 (2018).
768 8 Hassan, R., Kreitman, R. J., Pastan, I. & Willingham, M. C. Localization of Mesothelin in
769 Epithelial Ovarian Cancer. *Appl. Immunohistochem. Mol. Morphol.* **13**, 243-247,
770 doi:10.1097/01.pai.00000141545.36485.d6 (2005).
771 9 Chang, M.-C. *et al.* Mesothelin enhances invasion of ovarian cancer by inducing MMP-7
772 through MAPK/ERK and JNK pathways. *Biochem. J.* **442**, 293-302,
773 doi:10.1042/bj20110282 (2012).
774 10 Tornos, C. *et al.* Expression of WT1, CA 125, and GCDFP-15 as useful markers in the
775 differential diagnosis of primary ovarian carcinomas versus metastatic breast cancer to
776 the ovary. *Am. J. Surg. Pathol.* **29**, 1482-1489,
777 doi:10.1097/01.pas.0000176429.88702.36 (2005).
778 11 Kriplani, D. & Patel, M. M. Immunohistochemistry: A diagnostic aid in differentiating
779 primary epithelial ovarian tumors and tumors metastatic to the ovary. *South Asian Journal*
780 *of Cancer* **02**, 254-258, doi:10.4103/2278-330x.119888 (2013).
781 12 Neunteufel, W. & Breitenecker, G. Tissue expression of CA 125 in benign and malignant
782 lesions of ovary and fallopian tube: a comparison with CA 19-9 and CEA. *Gynecol.*
783 *Oncol.* **32**, 297-302, doi:10.1016/0090-8258(89)90628-8 (1989).
784 13 Cox, T. R. The matrix in cancer. *Nature Reviews Cancer* **21**, 217-238,
785 doi:10.1038/s41568-020-00329-7 (2021).

15

786 14 Bhat, R. & Bissell, M. J. Of plasticity and specificity: dialectics of the microenvironment
787   and macroenvironment and the organ phenotype. *WIREs Developmental Biology* **3**, 147-
788   163, doi:10.1002/wdev.130 (2014).
789 15 Roskelley, C. D. & Bissell, M. J. The dominance of the microenvironment in breast and
790   ovarian cancer. *Semin. Cancer Biol.* **12**, 97-104, doi:10.1006/scbi.2001.0417 (2002).
791 16 Mhawech-Fauceglia, P. *et al.* Stromal Expression of Fibroblast Activation Protein Alpha
792   (FAP) Predicts Platinum Resistance and Shorter Recurrence in patients with Epithelial
793   Ovarian Cancer. *Cancer Microenviron.* **8**, 23-31, doi:10.1007/s12307-014-0153-7 (2015).
794 17 Nissen, N. I., Karsdal, M. & Willumsen, N. Collagens and Cancer associated fibroblasts in
795   the reactive stroma and its relation to Cancer biology. *J. Exp. Clin. Cancer Res.* **38**, 115,
796   doi:10.1186/s13046-019-1110-6 (2019).
797 18 Saha, P. & Datta, K. Multi-functional, multicompartmental hyaluronan-binding protein 1
798   (HABP1/p32/gC1qR): implication in cancer progression and metastasis. *Oncotarget* **9**,
799   10784-10807, doi:10.18632/oncotarget.24082 (2018).
800 19 Longacre, M. *et al.* A Comparative Analysis of Genetic and Epigenetic Events of Breast
801   and Ovarian Cancer Related to Tumorigenesis. *Int. J. Mol. Sci.* **17**, 759,
802   doi:10.3390/ijms17050759 (2016).
803 20 Iyengar, M. *et al.* CDK4/6 inhibition as maintenance and combination therapy for high
804   grade serous ovarian cancer. *Oncotarget* **9**, 15658-15672,
805   doi:10.18632/oncotarget.24585 (2018).
806 21 Farley, J. *et al.* Selumetinib in women with recurrent low-grade serous carcinoma of the
807   ovary or peritoneum: an open-label, single-arm, phase 2 study. *The Lancet Oncology* **14**,
808   134-140, doi:10.1016/s1470-2045(12)70572-7 (2013).
809 22 McGivern, N. *et al.* Activation of MAPK signalling results in resistance to saracatinib
810   (AZD0530) in ovarian cancer. *Oncotarget* **9**, 4722-4736, doi:10.18632/oncotarget.23524
811   (2018).
812 23 Liston, D. R. & Davis, M. Clinically Relevant Concentrations of Anticancer Drugs: A Guide
813   for Nonclinical Studies. *Clin. Cancer. Res.* **23**, 3489-3498, doi:10.1158/1078-0432.CCR-
814   16-3083 (2017).
815 24 Ovejero, S., Bueno, A. & Sacristán, M. P. Working on Genomic Stability: From the S-
816   Phase to Mitosis. *Genes* **11**, 225, doi:10.3390/genes11020225 (2020).
817 25 Holder, J., Poser, E. & Barr, F. A. Getting out of mitosis: spatial and temporal control of
818   mitotic exit and cytokinesis byPP1 andPP2A. *FEBS Lett.* **593**, 2908-2924,
819   doi:10.1002/1873-3468.13595 (2019).
820 26 Aramburu, J., Ortells, M. C., Tejedor, S., Buxadé, M. & López-Rodríguez, C.
821   Transcriptional regulation of the stress response by mTOR. *Science Signaling* **7**, re2,
822   doi:10.1126/scisignal.2005326 (2014).
823 27 Dry, J. R. *et al.* Transcriptional Pathway Signatures Predict MEK Addiction and Response
824   to Selumetinib (AZD6244). *Cancer Res.* **70**, 2264-2273, doi:10.1158/0008-5472.can-09-
825   1577 (2010).
826 28 Fernandez, M. L. *et al.* Markers of MEK inhibitor resistance in low-grade serous ovarian
827   cancer: EGFR is a potential therapeutic target. *Cancer Cell Int.* **19**, 10,
828   doi:10.1186/s12935-019-0725-1 (2019).
829 29 Megyesi, J., Tarcsafalvi, A., Seng, N., Hodeify, R. & Price, P. Cdk2 phosphorylation of
830   Bcl-xL after stress converts it to a pro-apoptotic protein mimicking Bax/Bak. *Cell Death
831   Discovery* **2**, 15066, doi:10.1038/cddiscovery.2015.66 (2016).
832 30 Garon, E. B. *et al.* Identification of Common Predictive Markers of In vitro Response to
833   the Mek Inhibitor Selumetinib (AZD6244; ARRY-142886) in Human Breast Cancer and
834   Non-Small Cell Lung Cancer Cell Lines. *Mol. Cancer Ther.* **9**, 1985-1994,
835   doi:10.1158/1535-7163.mct-10-0037 (2010).
836 31 Sato, E. *et al.* Intraepithelial CD8+ tumor-infiltrating lymphocytes and a high
837   CD8+/regulatory T cell ratio are associated with favorable prognosis in ovarian cancer.
838   *Proc. Natl. Acad. Sci. U. S. A.* **102**, 18538-18543, doi:10.1073/pnas.0509182102 (2005).

16

839 32   Zhang, L. *et al.* Intratumoral T Cells, Recurrence, and Survival in Epithelial Ovarian
840   Cancer. *New Engl. J. Med.* **348**, 203-213, doi:10.1056/nejmoa020177 (2003).
841 33   Hamanishi, J. *et al.* Programmed cell death 1 ligand 1 and tumor-infiltrating CD8+ T
842   lymphocytes are prognostic factors of human ovarian cancer. *Proceedings of the National*
843   *Academy of Sciences* **104**, 3360-3365, doi:10.1073/pnas.0611533104 (2007).
844 34   Ye, Q. *et al.* CD137 Accurately Identifies and Enriches for Naturally Occurring Tumor-
845   Reactive T Cells in Tumor. *Clin. Cancer. Res.* **20**, 44-55, doi:10.1158/1078-0432.ccr-13-
846   0945 (2014).
847 35   Duhen, T. *et al.* Co-expression of CD39 and CD103 identifies tumor-reactive CD8 T cells
848   in human solid tumors. *Nat Commun* **9**, 2724, doi:10.1038/s41467-018-05072-0 (2018).
849 36   Simoni, Y. *et al.* Bystander CD8+ T cells are abundant and phenotypically distinct in
850   human tumour infiltrates. *Nature* **557**, 575-579, doi:10.1038/s41586-018-0130-2 (2018).
851 37   Canale, F. P. *et al.* CD39 Expression Defines Cell Exhaustion in Tumor-Infiltrating
852   CD8+T Cells. *Cancer Res.* **78**, 115-128, doi:10.1158/0008-5472.can-16-2684 (2018).
853 38   Jansen, C. S. *et al.* An intra-tumoral niche maintains and differentiates stem-like CD8 T
854   cells. *Nature* **576**, 465-470, doi:10.1038/s41586-019-1836-5 (2019).
855 39   Yu, G. & Wang, J. Significance of hyaluronan binding protein (HABP1/P32/gC1qR)
856   expression in advanced serous ovarian cancer patients. **94**, 210-215,
857   doi:10.1016/j.yexmp.2012.06.007 (2013).
858 40   Yu, H. *et al.* Elevated expression of hyaluronic acid binding protein 1
859   (HABP1)/P32/C1QBP is a novel indicator for lymph node and peritoneal metastasis of
860   epithelial ovarian cancer patients. *Tumor Biol.* **34**, 3981-3987, doi:10.1007/s13277-013-
861   0986-6 (2013).
862 41   Barnett, B., Kryczek, I., Cheng, P., Zou, W. & Curiel, T. J. Regulatory T cells in ovarian
863   cancer: biology and therapeutic potential. *Am. J. Reprod. Immunol.* **54**, 369-377,
864   doi:10.1111/j.1600-0897.2005.00330.x (2005).
865 42   Chen, H. *et al.* Short-term organoid culture for drug sensitivity testing of high-grade
866   serous carcinoma. *Gynecol. Oncol.* **157**, 783-792, doi:10.1016/j.ygyno.2020.03.026
867   (2020).
868 43   Kopper, O. *et al.* An organoid platform for ovarian cancer captures intra- and interpatient
869   heterogeneity. *Nat. Med.* **25**, 838-849, doi:10.1038/s41591-019-0422-6 (2019).
870 44   Hill, S. J. *et al.* Prediction of DNA Repair Inhibitor Response in Short-Term Patient-
871   Derived Ovarian Cancer Organoids. *Cancer Discov.* **8**, 1404-1421, doi:10.1158/2159-
872   8290.CD-18-0474 (2018).
873 45   Valeriote, F. & van Putten, L. Proliferation-dependent cytotoxicity of anticancer agents: a
874   review. *Cancer Res.* **35**, 2619-2630 (1975).
875 46   Vasey, P. A. Resistance to chemotherapy in advanced ovarian cancer: mechanisms and
876   current strategies. *Br. J. Cancer* **89**, 23-28, doi:10.1038/sj.bjc.6601497 (2003).
877 47   Haygood, C. L. W. Ovarian cancer stem cells: Can targeted therapy lead to improved
878   progression-free survival? *World Journal of Stem Cells* **6**, 441, doi:10.4252/wjsc.v6.i4.441
879   (2014).
880 48   Bapat, S. A., Mali, A. M., Koppikar, C. B. & Kurrey, N. K. Stem and Progenitor-Like Cells
881   Contribute to the Aggressive Behavior of Human Epithelial Ovarian Cancer. *Cancer Res.*
882   **65**, 3025-3029, doi:10.1158/0008-5472.can-04-3931 (2005).
883 49   Deng, J. *et al.* Targeting epithelial-mesenchymal transition and cancer stem cells for
884   chemoresistant ovarian cancer. *Oncotarget* **7**, 55771-55788,
885   doi:10.18632/oncotarget.9908 (2016).
886 50   Liu, S. *et al.* NANOG regulates epithelial-mesenchymal transition and chemoresistance
887   through activation of the STAT3 pathway in epithelial ovarian cancer. *Tumor Biol.* **37**,
888   9671-9680, doi:10.1007/s13277-016-4848-x (2016).
889 51   Balmanno, K., Chell, S. D., Gillings, A. S., Hayat, S. & Cook, S. J. Intrinsic resistance to
890   the MEK1/2 inhibitor AZD6244 (ARRY-142886) is associated with weak ERK1/2
891   signalling and/or strong PI3K signalling in colorectal cancer cell lines. *Int. J. Cancer* **125**,
892   2332-2341, doi:10.1002/ijc.24604 (2009).

17

893 52 Lee, C. H. *et al.* Constitutive mTOR activation in TSC mutants sensitizes cells to energy
894   starvation and genomic damage via p53. *The EMBO journal* **26**, 4812-4823,
895   doi:10.1038/sj.emboj.7601900 (2007).
896 53 Vadysirisack, D. D., Baenke, F., Ory, B., Lei, K. & Ellisen, L. W. Feedback control of p53
897   translation by REDD1 and mTORC1 limits the p53-dependent DNA damage response.
898   *Mol. Cell. Biol.* **31**, 4356-4365, doi:10.1128/mcb.05541-11 (2011).
899 54 Leontieva, O. V. & Blagosklonny, M. V. DNA damaging agents and p53 do not cause
900   senescence in quiescent cells, while consecutive re-activation of mTOR is associated
901   with conversion to senescence. *Aging (Albany NY)* **2**, 924-935,
902   doi:10.18632/aging.100265 (2010).
903 55 Astle, M. V. *et al.* AKT induces senescence in human cells via mTORC1 and p53 in the
904   absence of DNA damage: implications for targeting mTOR during malignancy. *Oncogene*
905   **31**, 1949-1962, doi:10.1038/onc.2011.394 (2012).
906 56 Gajewski, T. F., Schreiber, H. & Fu, Y.-X. Innate and adaptive immune cells in the tumor
907   microenvironment. *Nat. Immunol.* **14**, 1014-1022, doi:10.1038/ni.2703 (2013).
908 57 Hwang, W. T., Adams, S. F., Tahirovic, E., Hagemann, I. S. & Coukos, G. Prognostic
909   significance of tumor-infiltrating T cells in ovarian cancer: a meta-analysis. *Gynecol.*
910   *Oncol.* **124**, 192-198, doi:10.1016/j.ygyno.2011.09.039 (2012).
911 58 Curiel, T. J. *et al.* Specific recruitment of regulatory T cells in ovarian carcinoma fosters
912   immune privilege and predicts reduced survival. *Nat. Med.* **10**, 942-949,
913   doi:10.1038/nm1093 (2004).
914 59 Leem, G. *et al.* 4-1BB co-stimulation further enhances anti-PD-1-mediated reinvigoration
915   of exhausted CD39+ CD8 T cells from primary and metastatic sites of
916   epithelial ovarian cancers. *Journal for ImmunoTherapy of Cancer* **8**, e001650,
917   doi:10.1136/jitc-2020-001650 (2020).
918 60 Przystal, J. M. *et al.* Targeting CSF1R Alone or in Combination with PD1 in Experimental
919   Glioma. *Cancers (Basel)* **13**, 2400, doi:10.3390/cancers13102400 (2021).
920 61 Walter, B. *et al.* Argyrin F Treatment-Induced Vulnerabilities Lead to a Novel Combination
921   Therapy in Experimental Glioma. *Advanced Therapeutics*, 2100078,
922   doi:10.1002/adtp.202100078 (2021).
923 62 Pirnia, F. *et al.* Novel functional profiling approach combining reverse phase protein
924   microarrays and human 3-D ex vivo tissue cultures: expression of apoptosis-related
925   proteins in human colon cancer. *Proteomics* **9**, 3535-3548, doi:10.1002/pmic.200800159
926   (2009).
927 63 Pawlak, M. & Carragher, N. O. Reverse Phase Protein Arrays elucidate mechanisms-of-
928   action and phenotypic response in 2D and 3D models. *Drug Discovery Today:*
929   *Technologies* **23**, 7-16, doi:10.1016/j.ddtec.2017.05.002 (2017).
930 64 Kresbach, G. M. & Pawlak, M. High Precision RPPA: Concept, Features, and Application
931   Performance of the Integrated Zeptosens Platform. *Adv. Exp. Med. Biol.* **1188**, 31-59,
932   doi:10.1007/978-981-32-9755-5_3 (2019).
933 65 Iglewicz, B. & Hoaglin, D. C. *How to detect and handle outliers*. (Milwaukee, Wis. :
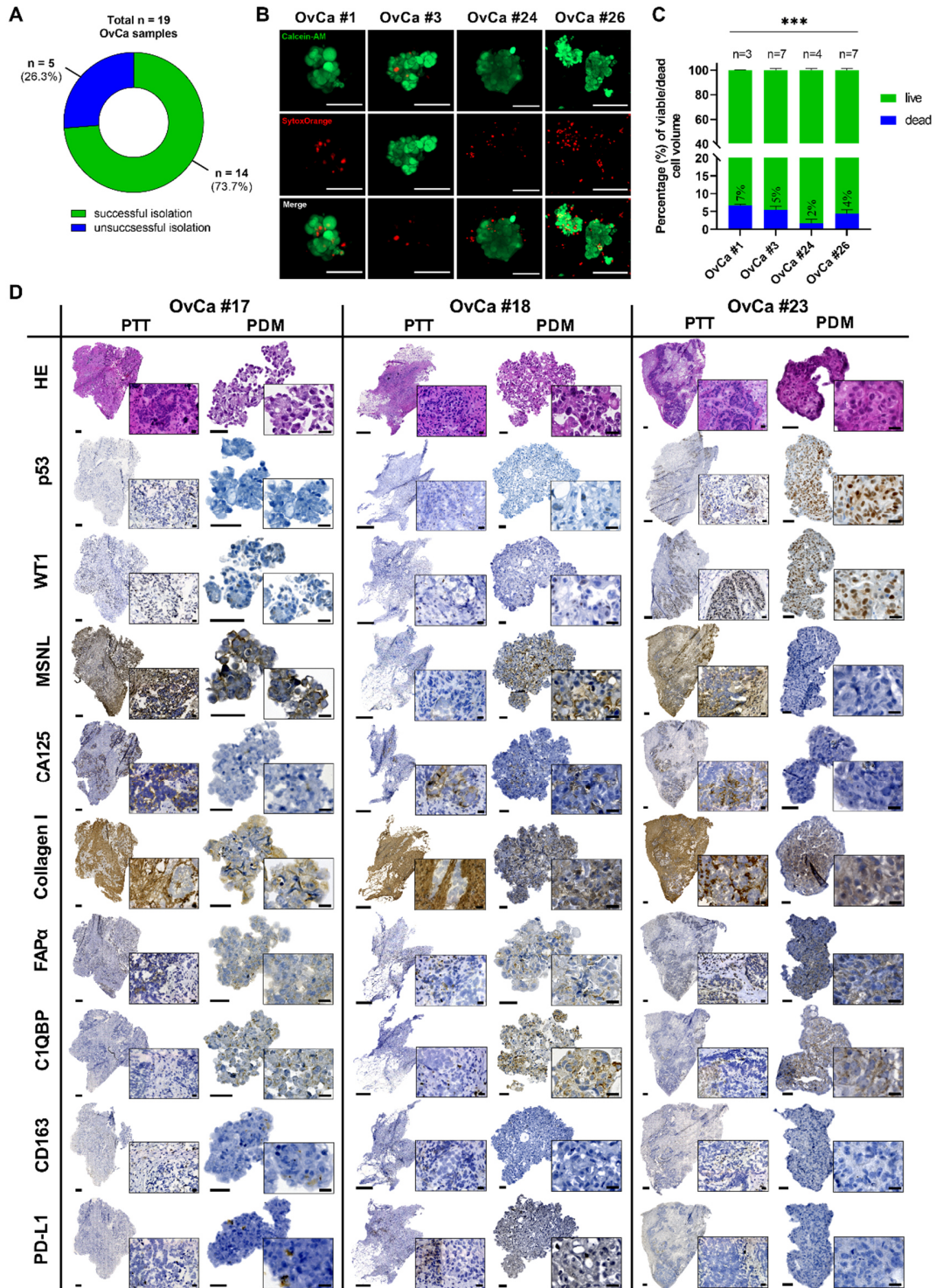934   ASQC Quality Press, 1993).

935

936

937

938

939

940

941   **Figures and Tables**

942
943

944 **Figure 1. Patient-derived 3D microtumors (PDM) derived from primary OvCa tumor**
945 **specimen show high viability and resemble histopathologocial features of the**
946 **corresponding PTT.** (**A**) Efficiency of isolating OvCa PDM from a total of *n* = 19 fresh primary
947 OvCa tumor tissues samples. PDM gained from *n* = 14 specimen with a success rate of 73.7%.
948 (**B**) Viability of OvCa PDM models. Exemplary 2D images from 3D projections of *n* = 4 OvCa
949 PDM models confirm high viability according to Calcein-AM (viable cells) and SYTOX™ Orange
950 (dead cells) staining. (**C**) Percentage of viable and dead cells in OvCa PDM. Viability was
951 assessed by an image-based analysis (see SI Methods) in *n* = 4 OvCa PDM models shown in
952 (B). Data are shown as mean values with SEM from at least *n* = 3 PDM of each model. *$*P* < 0.05,
953 **$**P* < 0.01, ***$***P* < 0.001, multiple paired t-test with Holm-Šídák's post hoc test. Scale bar 50 µm.
954 (**D**) Hematoxylin and Eosin (H&E) as well as immunohistochemical staining of OvCa PDM and
955 corresponding primary tumor tissue (PTT) sections. H&E stainings revealed features of malignant
956 cells (incl. giant cells with more than one nucleolus, hyperchromatic cells and high
957 nuclei:cytoplasma ratio) confirming the cancerous origin. Scale bars indicate 500 µm for PTT; 50
958 µm for PDM; 20 µm for magnifications (PTT and PDM). FAPα, cancer-associated fibroblast
959 protein alpha; C1QBP, hyaluronan binding protein; WT1, wilms tumor 1; MSNL, mesothelin.

960
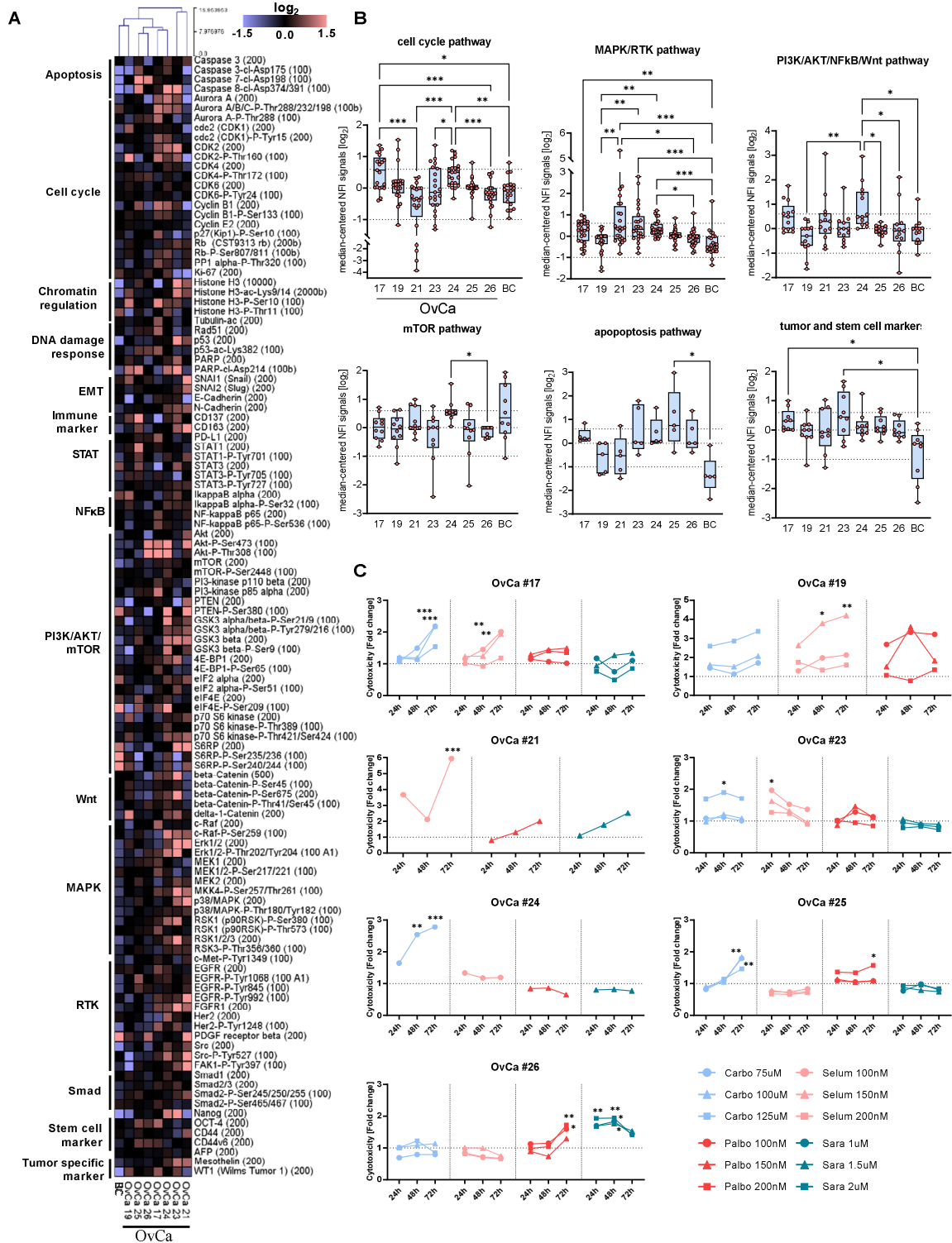
961 **Figure 2. RPPA protein profiling of OvCa PDM identifies significant differences in active**
962 **protein signaling pathways as molecular basis for OvCa PDM drug treatment responses.**
963 (**A**) Protein heat map covering 116 analytes analyzed in OvCa PDM (n = 7) and BC PDM (n = 1)
964 generated from sample sizes of n = 100-150 PDM. Protein abundances for each analyte are
965 displayed as median-centered, $\log_2$-transformed NFI signals. Samples were subjected to
966 hierarchical clustering using Euclidean distance (complete linkage). (**B**) Activation state of
967 different pathways in the different OvCa PDM models. Proteins related to an "active" pathway
968 were selected for each of the plotted pathways (see Table S4). Protein signals are shown as
969 median-centered, $\log_2$ transformed NFI signals. Dotted lines indicate $\log_2$ values of +0.6 (fold
970 change of +1.5) and -1 $\log_2$ (fold change of -0.5). Data are shown as box and whiskers plots with
971 minimum and maximum range. *P < 0.05, **P < 0.01, ***P < 0.001, Kruskal-Wallis test with
972 Dunn's post hoc test. (**C**) Cytotoxicity measurement of OvCa PDM treated with standard
973 platinum-based chemotherapy (carbo 75-125 µM) and/or targeted therapy (selum 100-200 nM,
974 palbo 100-200 nM, sara 1-2 µM). Four replicates per treatment with n = 15 PDM per well were
975 performed and measured after 24 h, 48 h and 72 h. Signals were measured as RFU (Relative
976 Fluorescent Unit), background corrected and normalized to vehicle control (DMSO). In case of
977 palbociclib to H_2O control. Data are shown as mean values. Statistical significances compared to
978 vehicle control or H_2O are shown. *P < 0.05, **P < 0.01, ***P < 0.001, Two-way ANOVA with
979 Bonferroni's multiple comparison test. Carbo: carboplatin; Selum: selumetinib; Palbo: palbociclib;
980 Sara: saracatenib
981
982
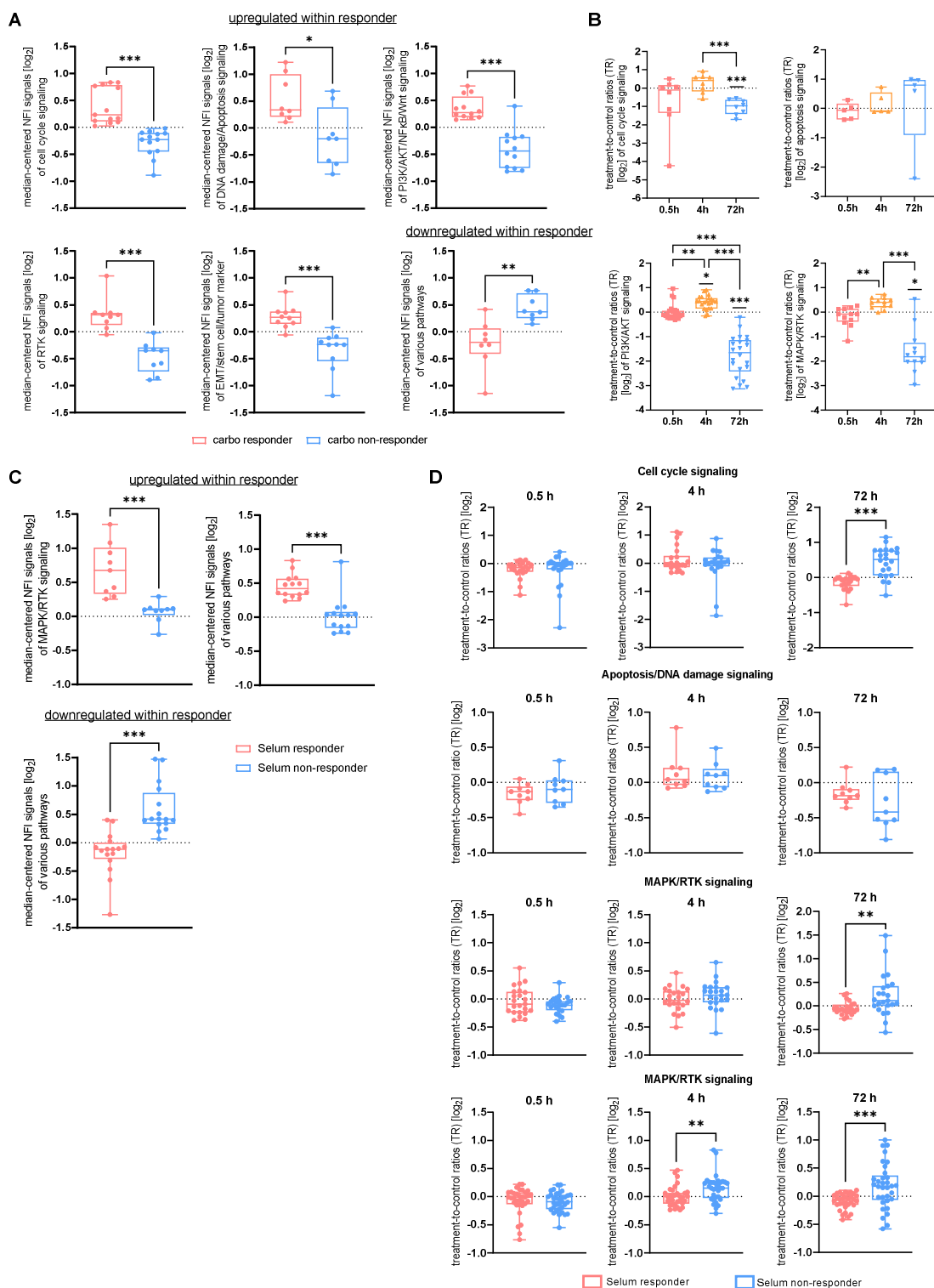
985 **Figure 3. Carboplatin and selumetinib drug response in OvCa PDM correlates with the**
986 **activity of diverse signaling pathways.** (**A, C**) Signaling pathway activation in carboplatin (**A**)
987 and selumetinib (**C**) responder vs. non-responder OvCa PDM. Proteins were sorted according to
988 their pathway affiliation and according to upregulation or downregulation within responder group.
989 *$P < 0.05$, **$P < 0.01$, ***$P < 0.001$, Mann-Whitney-U-test. R, responder; Non-R, Non-responder.
990 (**B**, **D**) Proteomic on- and off-target pathway effects in carboplatin- and selumetinib-treated OvCa
991 PDM analyzed by RPPA. Treated PDM were analyzed from an immediate (0.5 h), an early (4 h)
992 and a late (72 h) treatment time. For each time point, protein values are displayed as $\log_2$-
993 transformed treatment-to-control signal ratios (TR) calculated from NFI signals of treated PDM
994 and corresponding vehicle control (DMSO). (**B**) OvCa #24 PDM were treated with 75 μM
995 carboplatin. Only proteins with >50% differential protein abundance compared to vehicle control
996 were selected, sorted according to pathway affiliation and plotted as box whisker plots. Significant
997 differences between time points and vehicle control were measured. Straight lines above plots
998 indicate statistical significances compared to vehicle control. *$P < 0.05$, **$P < 0.01$, ***$P < 0.001$,
999 One-way ANOVA using nonparametric Kruskal-Wallis with Dunn's ad hoc test. (**D**) Proteomic on-
1000 and off-target pathway effects in selumetinib (100 nM) treated PDM. Selumetinib responder and
1001 non-responder PDM models were grouped. Only proteins with greater than 100% differential
1002 protein abundance between responder and non-responder PDM models were plotted according
1003 to signaling pathway affiliation. *$P < 0.05$, **$P < 0.01$, ***$P < 0.001$, Mann-Whitney U-test.

1004
1005
1006
1007
1008
1009
1010
1011
1012
1013
1014

24
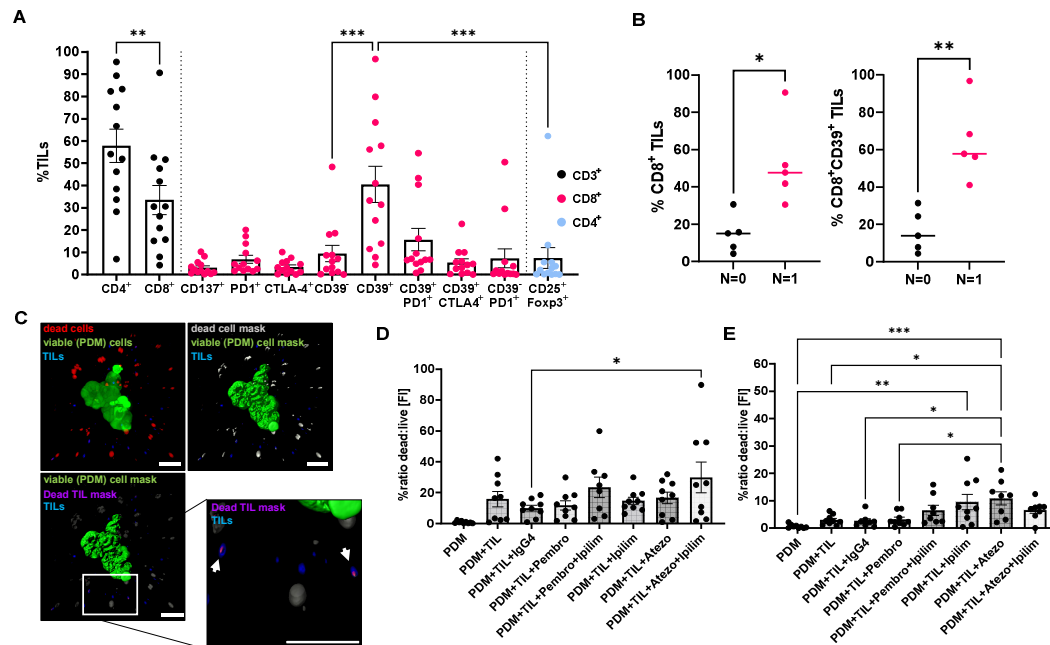
1015

Figure 4. CPI treatment in OvCa PDM-TIL co-cultures increased functional TIL killing effects. Autologous TIL populations were isolated and expanded from OvCa tissue specimen. (**A**) Percentages of different TIL populations within CD3, CD8 and CD4 positive T cells of different models were quantified by multicolor flow cytometry. Data are shown as means ± SEM of at least n = 10 OvCa samples. *P < 0.05, **P < 0.01, ***P < 0.001, ANOVA with Holm-Šídák's post hoc test. (**B**) Percentages of CD8^{+} and CD8^{+}CD39^{+} TILs in OvCa patients with lymph node spread (N = 1) and without lymph node spread (N = 0). All points with median are shown. *P < 0.05, **P < 0.01, Mann-Whitney-U-test. (**C-E**) Killing effects of autologous TILs on corresponding PDM in co-cultures treated with immune checkpoint inhibitors (CPI). (**C**) PDM killing effects were measured in an image-based assay format as ratio of fluorescent intensities (FI) of dead cells vs. live PDM cells. Per treatment n = 3 PDM in three replicates were analyzed. Masks for viable PDM (Calcein-AM staining), dead cells (SYTOX™ Orange dead cell staining) and TILs (CellTracker™ Deep Red staining) were applied using Imaris 8.0 software. Scale bars indicate 50 µm. FI from TILs were subtracted from the total dead FI. TILs of OvCa #24 (**D**) and #26 (**E**) were co-cultured with *n* = 15 PDM using an E:T ratio of 4:1 and treated with CPI either alone or in combination. *P < 0.05, **P < 0.01, ***P < 0.001, ANOVA with Holm-Šídák's post hoc test. Pembro: pembrolizumab 60 µg/ml; Ipilim: ipilimumab 50 µg/ml; Atezo: atezolizumab 50 µg/ml.

1033